Angle-Resolved Fluorescence of a Dye Coupled to a Plasmonic Nanohole Array

Francesco Floris *, Margherita Angelini *, Eliana Manobianco, Paola Pellacani, Valentina Tolardo, Franco Marabelli

Posted Date: 19 March 2024

doi: 10.20944/preprints202403.1082.v1

Keywords: organic dye; plasmon enhanced fluorescence; angular dispersion spectroscopy

Article

Angle-Resolved Fluorescence of a Dye Coupled to a Plasmonic Nanohole Array

Francesco Floris [1,*], Margherita Angelini [1,*], Eliana Manobianco [2], Paola Pellacani [2], Valentina Tolardo [2] and Franco Marabelli [1]

[1] Department of Physics, University of Pavia, Via Bassi 6, 27100 Pavia, Italy; franco.marabelli@unipv.it
[2] Plasmore S.r.l, Via Vittorio Emanuele II 4, 27100 Pavia, Italy; emanobianco.plasmore@gmail.com (E.M); ppellacani.plasmore@gmail.com (P.P); vtolardo.plasmore@gmail.com (V.T)
* Correspondence: francesco.floris@unipv.it (F.F.); margherita.angelini01@universitadipavia.it (M.A)

Featured Application: Resorting to gold nanohole arrays, it is possible to engineer multiplexed, label-free biosensing devices based on both plasmon-enhanced fluorescence and surface plasmon resonance detection methods. This has to be done by properly optimizing the gold nanohole array plasmonic response in combination with the fluorophore features, and consequently choosing the optimal measurement configuration for both the sensing methods.

Abstract: Gold nanohole arrays are periodic metastructures gathering huge interest for biosensing applications. The grating-like structure defines their plasmonic mode features and their angular dispersion can be used to highlight efficiently their interaction with the fluorescence emission of a properly tuned fluorophore. Resorting to a properly tuned/engineered/optimised plasmonic nanohole array and a commercial organic dye, we performed an accurate resolved angle-resolved optical characterization. The plasmonic fingerprints was consequently identified as a modification of the dye photoluminescence signal in terms of both spectral redistribution and enhancement. Interestingly, by analyzing the results, an advantageous measurement configuration can be identified to better engineer a suitable platform for efficiency maximization in plasmon-enhanced fluorescence-based applications. Therefore, the coupling mechanism with the plasmonic modes, and nanostructure properties can be carefully co-optimized.

Keywords: organic dye; plasmon enhanced fluorescence; angular dispersion spectroscopy

1. Introduction

The study of fluorescence and its dependence on the local environment has been investigated for long time [1,2]. In particular, the deposition of a dye on a surface and its interaction with the surroundings has been theoretically and experimentally investigated [3], for metallic surfaces [4]. This topic gathers a huge interest [5], in particular, thanks to the enhancement effects [6], crucial for technologically relevant applications such as (bio)molecule sensing. In this framework, the concept of optimal critical distance between the dye and the metal surface needs to be introduced: for small distances, the Förster quenching process prevails suppressing the fluorescence signal, whereas for large separation distances the enhancement is reduced until it is lost [6]. Nevertheless, in several studies dealing with different metallic platforms, such a constraint has been put into discussion and somewhere relaxed. [7–10]. As a result, beyond the field enhancement provided by the metal and acting on the dye pumping and/or emission processes, the efficiency depends mostly on the coupling between the plasmonic excitation with the far field radiation. In this regard, a wide amount of studies and applications concerning plasmon-enhanced fluorescence (PEF) has been performed using metallic nanoparticles, likely because plasmonic localized resonances can be easily optically excited and detected [11–15]. Instead, the use of metallic surfaces poses many constraints regarding the specific optical configuration to be used for exploiting the plasmonic resonances: in the case of thin layers a prism must be used; for corrugated surfaces or gratings, the diffraction must be considered

 doi:10.20944/preprints202403.1082.v1

[5,16–19]. Nevertheless, several applications have been developed using gold nanohole arrays (GNA) exploiting the capability of this particular kind of structure in tailoring the pumping and/or the emission features [20–23]. Interestingly, the angular distribution of the fluorescence signal with respect to the surface orientation has also been considered in some cases. Anyway, a complete study of the connection between the angle-dependent plasmonic behavior either in the pump as well as in emission, and the dye features has been performed in ref. [24] although it is focused on a single plasmonic delocalized resonance. At the same time, the majority of the most recent papers on this topic are focused on specific bio-detection problem with an empirical approach [13,25–28]. In this view, the present work is aimed at verifying the suitability of a GNA for engineering a comprehensive PEF platform. The GNA exhibits an optical response determined by a mix of either localized-, i.e. localized surface plasmon resonances (LSPRs), or propagating-, i.e. surface plasmon polaritons (SPPs), modes [29,30]. The GNA was developed by Plasmore Srl as a surface plasmon resonance (SPR) sensor [31]. Within the EU Horizon2020 h-ALO project [32] the GNA has been considered for the development of a double-detection sensor combining both SPR and PEF [33,34].

Therefore, we identified two main goals deserving our interest:

1. To analyze the spectral weight of fluorescence mediated by plasmonic resonance behavior and its angular dispersion;
2. To define the enhancement factor for each measurement configuration.

2. Materials and Methods

2.2. Nanofabrication of the Plasmonic Metasurface

The PEF platform is the GNA consisting of an hexagonal array of PMMA/air nanoholes, embedded in an optically thick gold layer deposited on a glass substrate [29]. The nanofabrication protocol is based on a combination of colloidal lithography and plasma-based processes. Cleaned SiO_2 microscope slides were activated under glow discharge for 15 min, and then a silanization process was performed. Thus, the silanized SiO_2 was coated with a 180 nm thick layer of polymethyl methacrylate (PMMA) using a spin coater. Consequently, a monolayer of polystyrene nanoparticles (diameter = 500 nm) was assembled and transferred on top of the PMMA layer using the Langmuir Blodgett technique. This monolayer was then conditioned via O_2 plasma etching to nanostructure the underlying PMMA layer. Consequently, a gold layer was deposited by magnetron sputtering with the same nominal thickness as the PMMA layer. The residual of the nanosphere mask was lifted off resorting to an isopropanol bath under ultrasonication. Finally, thermal treatment at 300°C for about one hour was performed to improve the stability of the gold layer. Surfaces fabricated have been characterized by resorting to the SEM technique. The gold ring surrounding the top of each hole is about 30 nm in height. A SEM image is reported in Figure 1, showing a very well ordered nanohole array, with a pitch around 460 nm.

 doi:10.20944/preprints202403.1082.v1

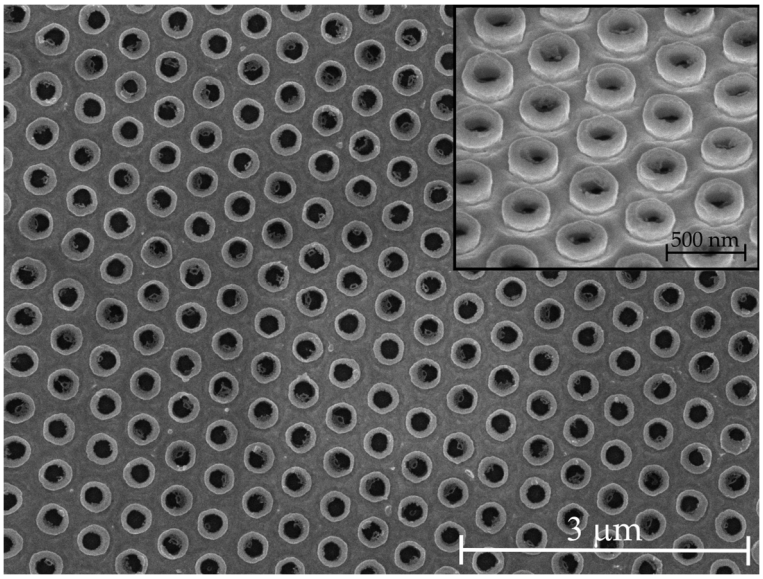

Figure 1. Scanning electron microscope image of the plasmonic metasurface.

2.2. Dye Deposition

ATTO700 dye was selected to provide a distinct spectral overlap between the dye fluorescence absorption and emission bands and plasmonic features observed [33,34]. The dye was deposited by drop-casting on the GNA and, in parallel, on a bare SiO_2 slide taken as a reference. To provide both uniformity and stability, alternating positively and negatively charged polyelectrolyte layers (PEL) were deposited on the targeted surface before the dye deposition process.

Operatively, a poly(styrene) sulfonate at 2% and a poly(diallyldimethylammonium) chloride at 2% solutions are alternatively deposited on the plasmonic metasurface, as shown in Figure 1. After each deposition step, the sample is washed with MilliQ water and dried under nitrogen flow. In this way, the PEL layers are stacked on the sample surface. The substrate charge has been considered in the deposition procedure: positive for the PEF platform and negative for the SiO_2 one. Therefore, two layers on the PEF platform were deposited and three in the SiO_2 case. Consequently, the PEL coverage thickness is estimated to be 4 nm for the PEF platform and 6 nm for the SiO_2 sample.

Finally, an 80 µMol aqueous solution of ATTO700 is deposited by drop-casting [35,36]. In this way, dye molecules are supposed to form a uniform single layer over the sample surface. Panel (a) of Figure 2 reports the PEF platform stack layout.

 doi:10.20944/preprints202403.1082.v1

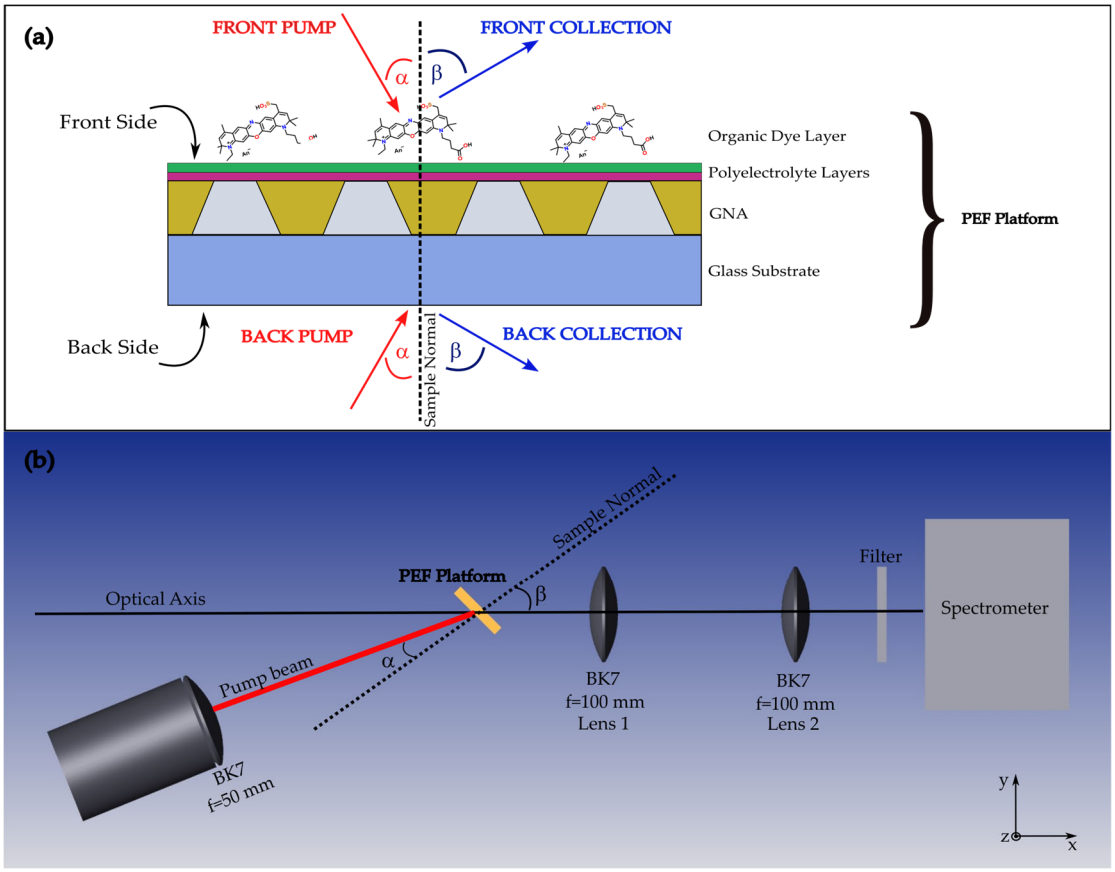

Figure 2. Panel (a): PEF platform stack layout and fluorescence measurement configurations. Panel (b): Scheme of the custom optical setup for either pumping (α) or collection (β) angle-resolved fluorescence measurements.

2.2. Experimental Optical Setups

A custom setup was realized to perform angle-resolved photoluminescence measurements for four different pumping and collection configurations. To better distinguish the different measurement configurations, two sides of the PEF platform are defined in panel (a) of Figure 2, i.e. the front and back sides. A schematic of the setup is shown in panel (b) of Figure 2.

This setup includes two independent custom pump and sample holder that allows for the autonomous selection of either the pumping or collection angles relative to the optical axis indicated as α and β respectively in panel (b) of Figure 2.

Specifically, a 632nm continuous-wave (CW) He-Ne laser coupled to a standard multimode optical fiber was employed as the source. The laser beam was focused on the sample's rotation axis using a BK7 lens with a focal length of 5 cm resulting in a 1 mm^2 spot diameter with a measured power of 10 mW.

Two BK7 lenses (Lens 1 and 2 in Figure 2) having the same focal length of 10 cm, were used to collect the fluorescence signal over an angle of 15 degrees.

An Oriel Multispec spectrograph equipped with a 600 lines/mm grating and a Thorlabs LC-100/M line camera was exploited for detection. To filter out the pumping laser line, a FELH0650 Thorlabs high-pass filter was placed before the 200 μm spectrograph slit.

The fluorescence signal was collected following two different measurement schemes, where the pumping angle alpha (α) and the collection angle beta (β) were changed. In the first one, α was varied relative to the plasmonic surface normal axis, while β was kept fixed. In the second scheme, β was spanned while maintaining α constant. In both configurations, the angle variation was set to 5°. To improve the collection resolution, a measurement at a fixed pumping angle was performed by using a single lens arrangement for the collection with an acceptance angle of 5°.

 doi:10.20944/preprints202403.1082.v1

The reflectance (R) and transmittance (T) data were collected using a commercial Fourier transform spectrometer Bruker IFS66S coupled to a custom micro reflectometer. Broadband (500 nm to 1000 nm) variable-incidence-angle R and T measurements were performed illuminating the sample from both front and back sides with a resolution of 16 cm^{-1}. A Glan-Taylor polarized was used to select the TE or TM spectral components.

3. Results

The measured fluorescence spectra of the PEF platform are presented in Figure 3. The configuration with the pump on the front side, panels (a) and (b) of Figure 3, shows a systematically higher intensity compared to pumping from the back side. By changing the pumping angle, the spectra intensity varies, whereas the spectral shape is mainly unaffected. In fact, the fluorescence maximum intensity is showing a decrease when pumping from the front side, Figure 3, panel (a); when pumping from the back side, Figure 3, panel (c), the fluorescence maximum intensity increases from 0° to 20° and then decreases. On the other hand, the spectral shape is mainly unaffected, displaying an emission maximum around 730 nm, which conserves the spectral position independently on the pumping angle.

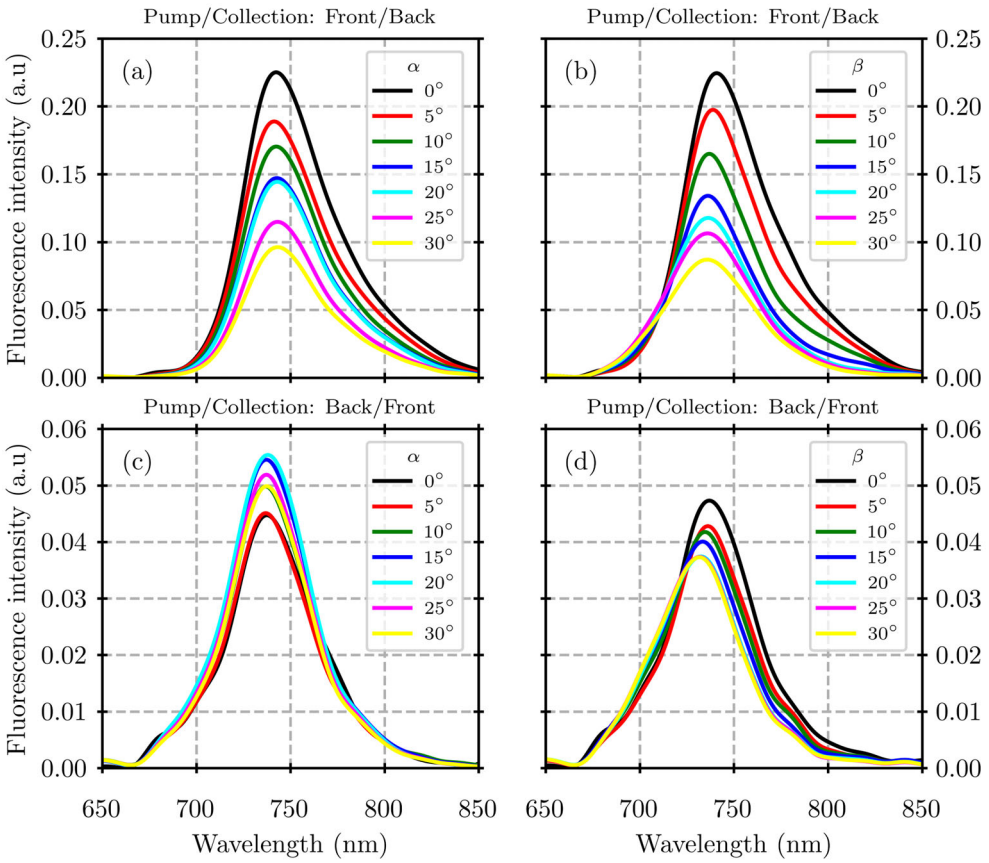

Figure 3. Variable-angle fluorescence spectra measured on the PEF platform by impinging and collecting on opposite sides. Panels (a) and (b) report the spectra collected when illuminating from the front side and collecting from the back one. Panels (c) and (d) refer to the pumping on the back side and collection from the front one. Spectra are shown as a function of the pumping angle α in panels (a) and (c), whereas of the collection angle β in panels (b) and (d).

On the contrary, considering the variation in collection angle, an evident reshape of the spectra is observed. As shown in panels (b) and (d) of Figure 3, the fluorescence emission maximum exhibits a progressive redistribution of the spectral shape towards lower wavelengths, together with an intensity decrease. The effect is more evident regarding the configuration of pumping from the front side and collecting from the back side.

 doi:10.20944/preprints202403.1082.v1

A consistent behavior of the fluorescence emission spectra is also observed when pumping and collection both insist on the same side (front/front or back/back). Figure 4 reports the results obtained for these configurations. In this case, the front/front measurements exhibit the largest fluorescence intensities, whereas the back/back ones are roughly one-third lower in intensity. Also, in this case, the spectral shape remains substantially unchanged when the pumping angle is varied, displaying a maximum around 730 nm. Starting from the lowest collection angle of 10°, the fluorescence maximum intensity monotonically decreases down to 45° for the front configuration (panel (a), Figure 4), while maintains its value up to 30° to lower again for the back/back configuration (panel (c), Figure 4).

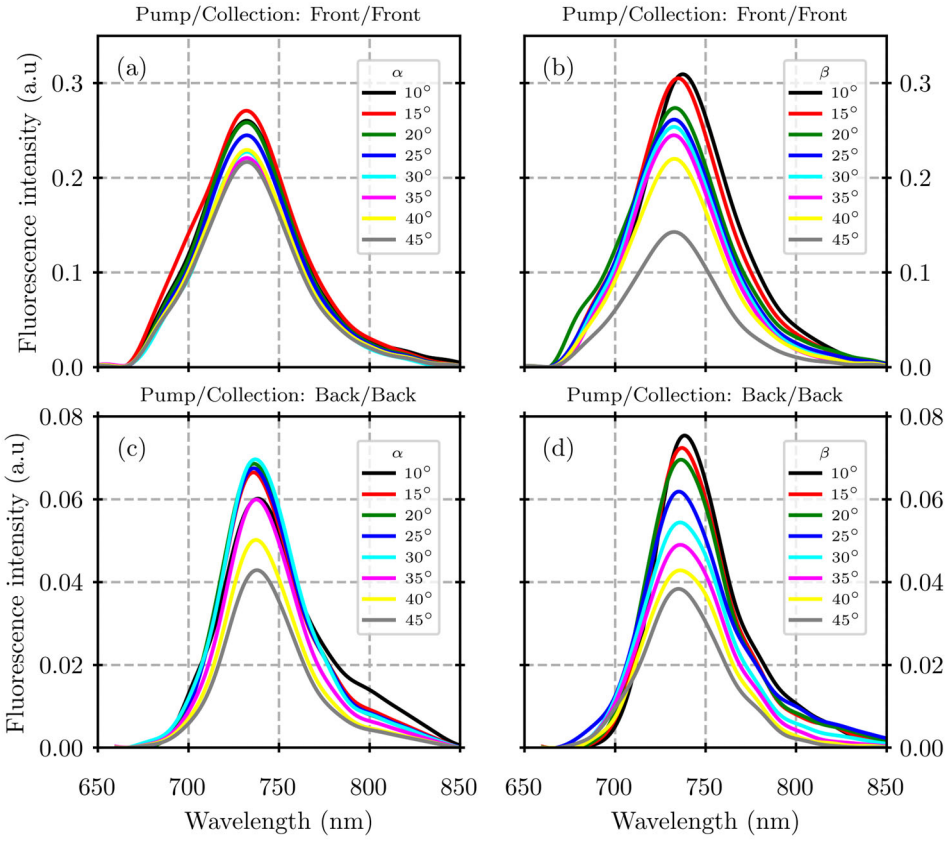

Figure 4. Variable-angle fluorescence spectra measured on the PEF platform by impinging and collecting from the same side. Panels (a) and (b) report the spectra corresponding to the front-side measurements. Panels (c) and (d) report the spectra corresponding to the back side ones. Spectra are shown as a function of the pumping angle α in panels (a) and (c), whereas of the collection angle β in panels (b) and (d).

A shift and a reshape of the spectral curves can be observed also in this case by varying the collection angle. In fact, for both the front/front and back/back configurations, panels (b) and (d) of Figure 4, respectively, the fluorescence spectra show a redistribution of their shape towards lower wavelengths, exhibiting a blue shift of the fluorescence maximum. So, by comparing the results corresponding to the different measurement configurations, it results that the side on which the pumping occurs is determining the intensity of the response. Instead, the spectral shape is mainly affected by the collection angle, independently of the chosen configuration.

The dispersion of SPPs can be identified by a comparison between the experimental R behavior and the theoretical SPPs model (see Appendix A1), depicted by the dotted curves in Figure 6. Here, the black lines in panel (d) can be ascribed to the SPPs related to the Au/SiO_2 interface and can be clearly observed when measuring from the back.

To better highlight the complex plasmonic response of the GNA, that can be associated with maxima and minima in the optical spectra, in Figure 5 are reported the second derivative of the reflectance (R) spectra (see Appendix A2, Figure A1) as function of the incidence angle [30]. The first

 doi:10.20944/preprints202403.1082.v1

row of Figure 5 (panels (a) and (b)) result from the TE and TM R spectra acquired impinging and collecting from the front side, while panels (c) and (d) from the back side, respectively. The dispersion behavior of the spectral features can be clearly observed and several different polaritonic branches can be recognized. The same behavior can be recognized also in transmittance (T), as shown in Appendix A1.

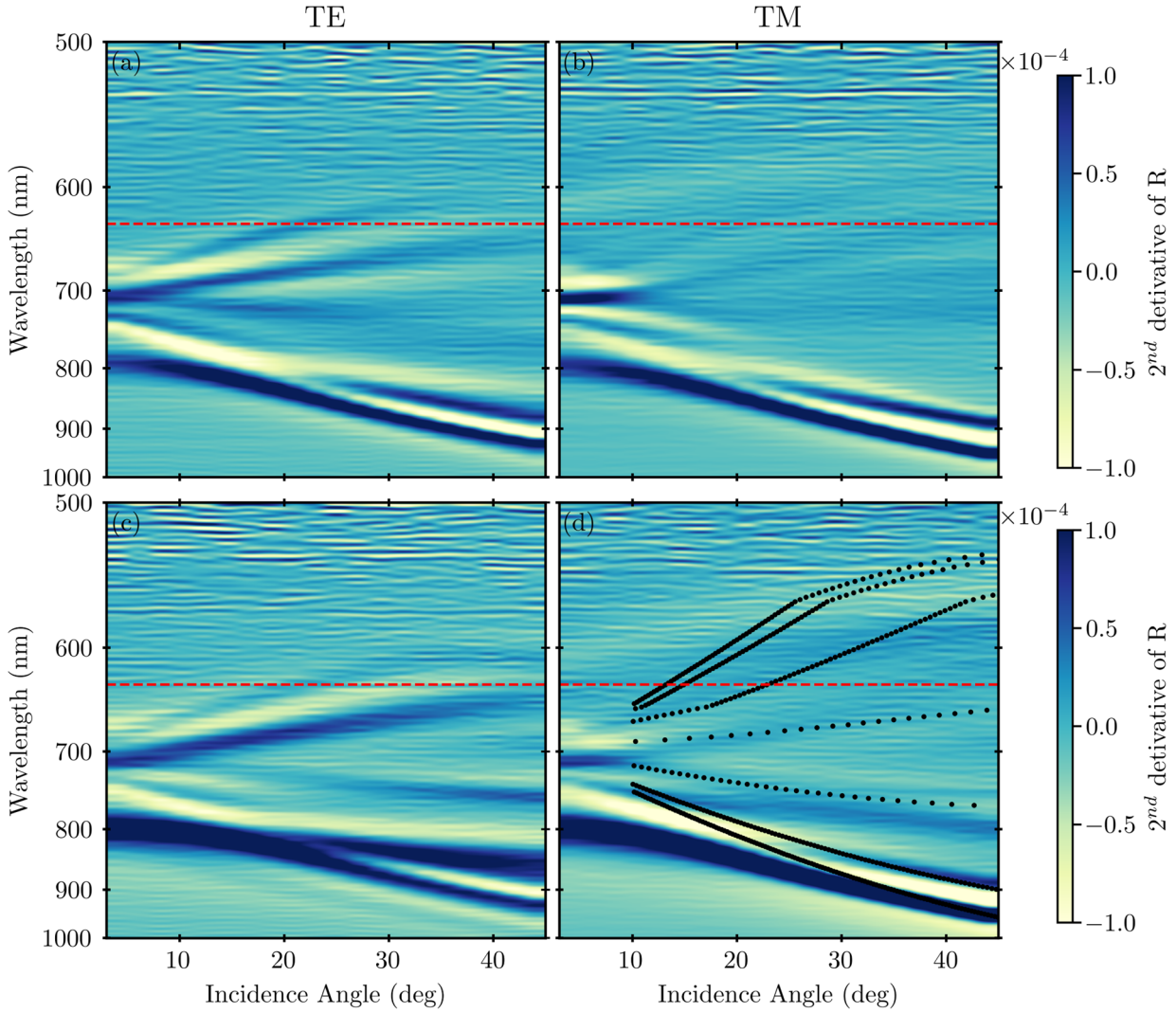

Figure 5. Second derivative of variable-incidence-angle R spectra for both TE and TM polarization. Panels (a) and (b) display the curves resulting from the spectra measured by impinging from the front side, while panels (c) and (d) from the back side, respectively. The red dashed line indicates the He-Ne pumping at 632 nm. The black curves in panel (d) are the SPP dispersion branches calculated with the model in Appendix A2 at the back side.

To identify the SPP dispersion, the calculated dispersion curves have been compared with the R spectra measured in the TM configuration. On the other hand, the R spectra in TE configuration had better show instead the LSPR modes. At the lowest angles, below 15°, a superposition of both LSPR and SPP modes is noticeable, together with the photonic band gap opening at about 680 nm, corresponding to a simultaneous minimum in T and a maximum in R. Besides, around 0° at 800 nm an evident optical branch can be observed with almost no dispersion until 10° and an evolution that coincides with the lowest SPP mode trend for larger angles. It is worth to notice how the laser excitation wavelength, indicated with the dashed red line in Figure 5, is crossing the GNA plasmonic modes around (15÷20) ° and (30÷40) °.

 doi:10.20944/preprints202403.1082.v1

4. Discussion

In consideration of the aforementioned optical behavior, a possible coupling between the GNA plasmonic modes and the organic dye features has been analyzed. As a starting point the fluorescence curves reported in Figure 3, panel (b), were plotted as a map considering the collection angle β and shown in Figure 6, panel (a).

By analyzing the level lines, the main structure changes asymmetrically with respect to the peak that is slightly blue shifting when increasing the angle β. At the same time, a shoulder around 770 nm higher wavelengths redshifts along the angle increase.

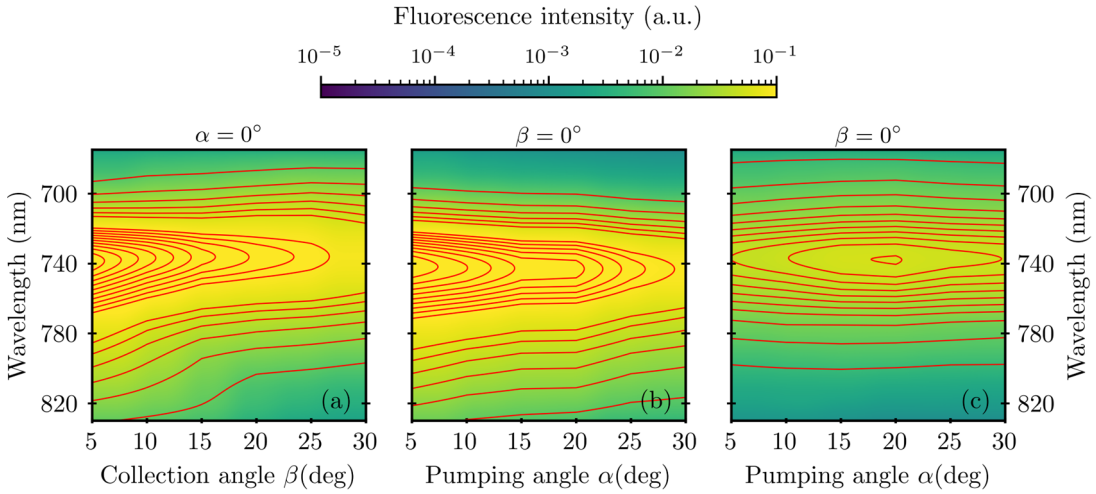

Figure 6. Fluorescence spectra maps measured by: (a) pumping at normal incidence from the front side and collecting from the back side as a function of the collection angle β; (b) pumping from the front side and collecting from the back side; and (c) pumping from the back side and collecting from the front side as a function of the pumping angle α.

Besides, looking at the pumping angle, no significant spectral changes in the curves are noted and the level lines follow the intensity variation. This variation undergoes an interruption between 15° and 20° when pumping from the front while shows a maximum when pumping from the back, Figure 6 panel (b) and (c) respectively. It is then clear that two different behaviors for the spectral evolution can be defined with respect to the collection and pumping angle. To better understand the dependence on the collection angle, the ratio of the fluorescence spectra at the different angles with respect to the one at normal incidence (collected at 0°) was considered and their plot are gathered up in a map reported in Figure 7, panel (a). For the sake of comparison, a subset of the second derivative of the TE-component of the T map measured impinging from the front side (see Appendix A2, Figure A2) is reported in panel (b) of Figure 7.

 doi:10.20944/preprints202403.1082.v1

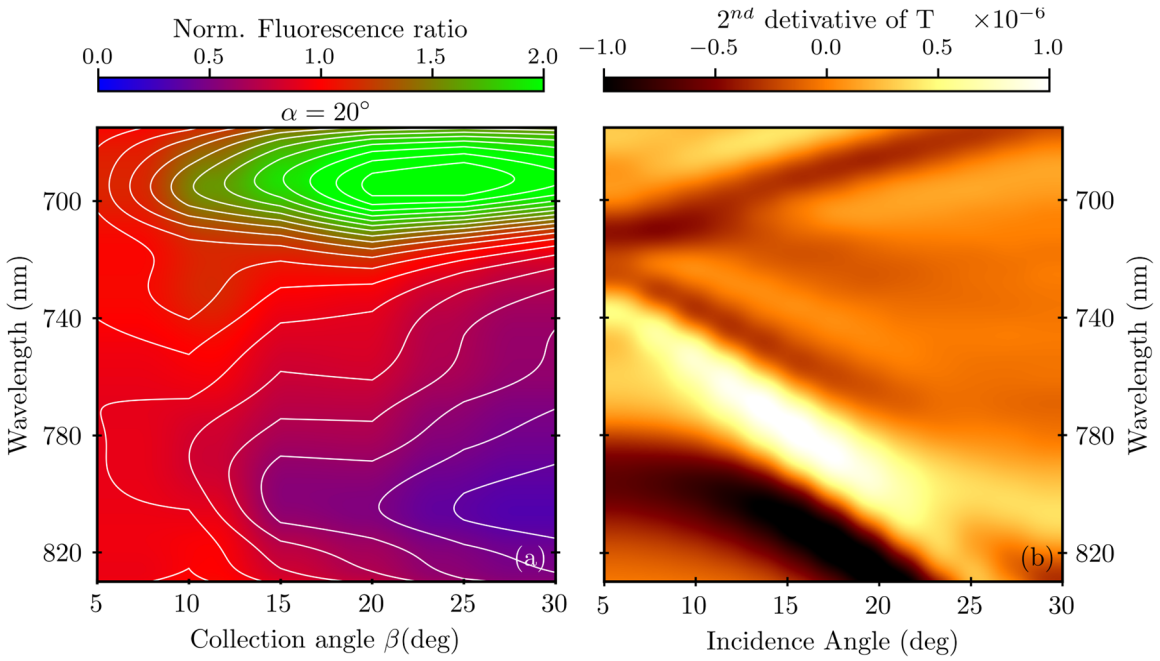

Figure 7. Map of the fluorescence spectral ratios at the different collection angles with respect to the one at normal incidence (collection angle 0°) for a pumping angle of 20°. In panel (a), second derivative of the T spectra (TE-component) in the fluorescence range detection. In panel (b), angular dependence of the absorbance evaluated at the pumping wavelength of 632 nm.

The dispersion of the spectral features can be identified in either the fluorescence or T maps highlighting the interplay between the GNA plasmonic modes and the fluorescence emission. This agrees with the literature where the explanation of the coupling mechanism is proposed in terms of excitation transfer between plasmonic resonances and dyes. According to Lackoviz [7] the emission efficiency is critically related to a direct interaction between the plasmonic modes with the far field radiation, either in absorption or in emission [8–10]. In our case, the structure periodicity guarantees the optical excitation and de-excitation of the LSPR and SPP plasmonic resonances.

Specifically, Chan et al. in reference [24] give an interpretation of the complexity of such an interplay, going beyond the pure Purcell effect due to field enhancement also report the collection of a fluorescence emission spectra showing the clear signature of a single plasmonic mode overlapped with the dye emission spectral range. Consistently, also in our case several different plasmonic modes contribute to reshape the fluorescence signal.

Instead, the influence of the pumping angle can be understood focusing on the absorbance (A), defined as A = 1-R-T, evaluated at the pumping laser wavelength of 632 nm. In Figure 8, A is presented for both front and back configurations as a function of the incident angle. For the sake of completeness, the variable-incidence-angle A maps are reported in Appendix A2, Figure A3. Regarding the front configuration, a tiny variation in A intensity is observed with a maximum in the range (15÷20) °. On the contrary, a relatively large variation occurs for the back configuration with a monotonic growth until 20° and a subsequent slowdown in growth for higher angles.

This is perfectly in line with the fluorescence results, when considered together with the increase in absorbance at 632 nm This can also be easily correlated to the crossing highlighted in Figure 5 between the laser excitation wavelength, with the GNA plasmonic modes around (15÷20) °.

This represents the fraction of energy that is stored into the plasmonic modes excited with a specific wavelength but different angles.

 doi:10.20944/preprints202403.1082.v1

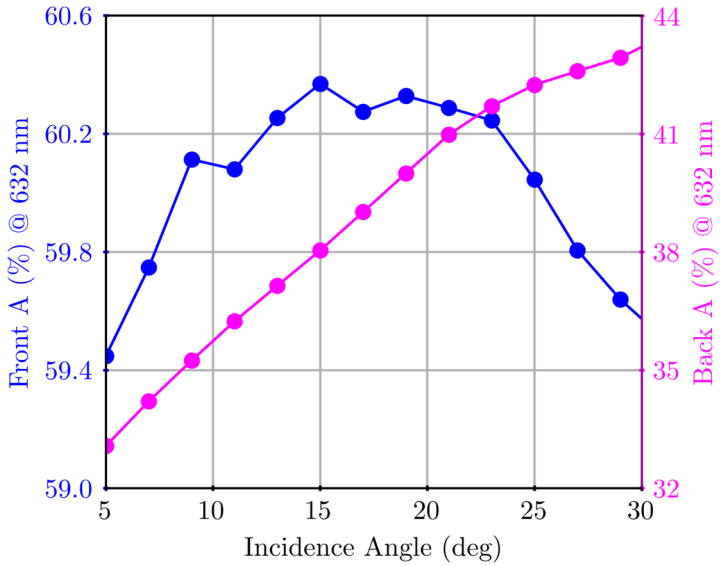

Figure 8. In panel (a), second derivative of the T spectra (TE-component) in the fluorescence range detection. In panel (b), angular dependence of the absorbance evaluated at the pumping wavelength of 632 nm.

In addition, also when focusing on the pumping mechanism, the plasmonic contribution to fluorescence is crucial. Remarkably, it can be noticed how the absorbance in the front configuration is roughly twice in intensity compared with the back configuration one. Therefore, it is not surprising that, as observed above, the largest fluorescence intensities are measured when pumping from the front side. Furthermore, the pumping wavelength is set within the spectral region below the band gap around 680 exciting selectively the plasmonic resonances lying down on the front surface, as reported in refs. [33,34]. These modes are characterized by a higher efficiency with respect to resonance centered around 780 nm (at 0°) thanks to a narrower bandwidth and a longer decay time [24].

In fact, the fluorescence signal is systematically and significantly larger when pumping from the front side. A contribution to the enhancement can be identified also in emission, in this case for wavelengths above the band gap, but it is much less effective.

The synergic combination of all the listed contributions to both pumping and collection, leads to an enhancement of the fluorescence signal. Figure 9 reports a comparison of the fluorescence signals for each of the four measurement configurations. The enhancement was evaluated as the ratio of the fluorescence spectra collected on the PEF platform with respect to the analogous measurement performed on the ATTO700 directly drop-casted on a bare SiO_2 substrate with PEL layers and no plasmonic metasurface underneath.

It can be clearly seen how the enhancement in the fluorescence signal for all the measurements performed with the support of the PEF platform is constantly relevant. Consistently with our findings, the highest enhancements are visible when pumping from the front, as visible in Figure 9 panels (a) and (b). In fact, the fluorescence signal collected from the PEF platform is enhanced roughly 40 and 60 times with respect to the bare glass reference considering the collection from the same side (the front) and the back side, respectively. Remarkably, the fluorescence signal is also enhanced when pumping from the back side and collecting from the back or the front sides, Figure 9 panels (c) and (d), respectively, but less efficiently, roughly about 20 times with respect to the reference.

 doi:10.20944/preprints202403.1082.v1

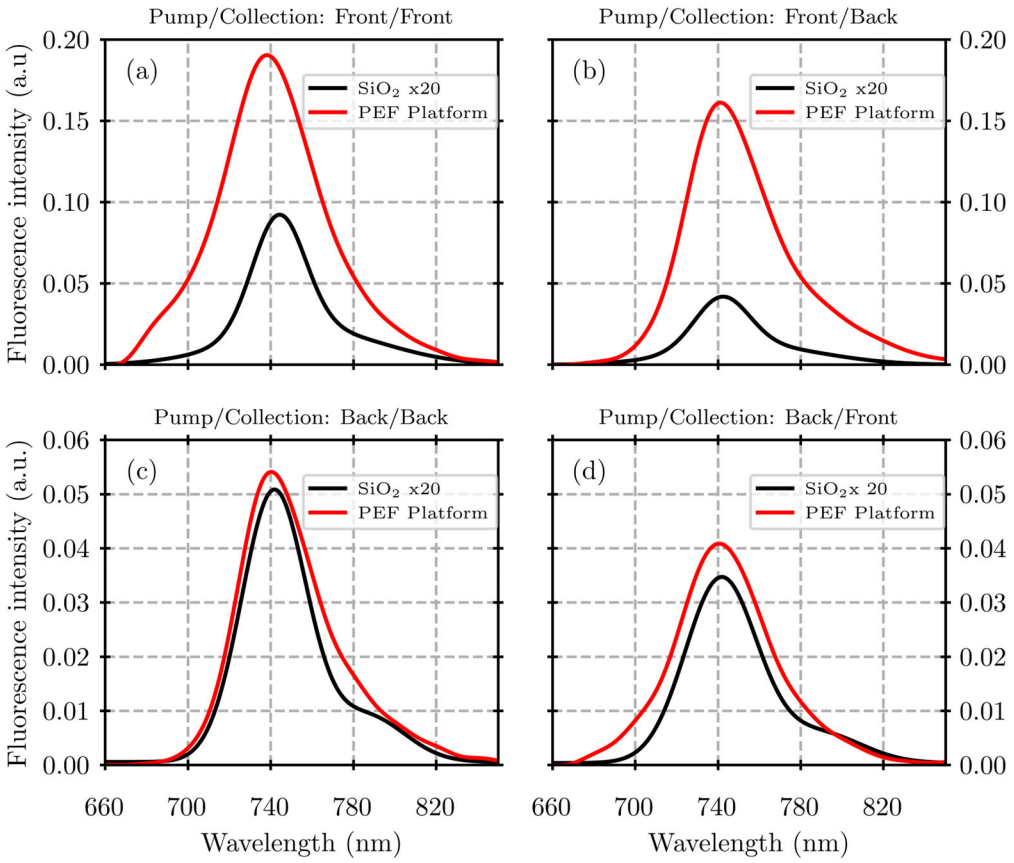

Figure 9. Fluorescence spectra measured on the PEF platform and on the reference glass slide, the signal is multiplied by a factor of 20, for the different measurement configurations. Pump and collection from the front (a) and back sides (c), respectively. (b) Pump from the front side and collection from the back side. (d) Pump from the back side and collection from the front side.

5. Conclusions

The combination of an off-the-shelf GNA, commonly used for SPR biosensing, and a commercial dye has been studied. The analysis was carried out in terms of spectral overlap between the complex (both LSPR and SPP) optical GNA response and the absorption and emission fluorophore features. The shape of the fluorophore contribution mainly dominates the fluorescence emission spectra. The signature of the underneath GNA can be anyway clearly recognized, particularly when considering their angular evolution. In addition, a remarkable fluorescence enhancement has been detected, depending on the specific measurement setup. Besides, the largest enhancement is observed by pumping from the front side, since the pumping beam is resonantly coupled to the plasmonic modes confined at the GNA-PEL interface, allowing the identification of a preferred measurement configuration.

Author Contributions: Conceptualization, F.M. and F.F.; methodology, F.F. and F.M.; validation, F.F., F.M. and M.A.; formal analysis, M.A.; investigation, E.M. and M.A.; resources, E.M., V.T. and P.P.; data curation, E.M. and M.A.; writing—original draft preparation V.T., E.M., M.A., F.F. and F.M.; writing—review and editing, F.M., F.F., E.M. and M.A.; visualization, F.M., F.F. and M.A.; supervision, F.M. and F.F.; project administration, F.F. and F.M.; funding acquisition, F.F. and F.M. All authors have read and agreed to the published version of the manuscript.

Funding: This research was co-funded by the European Union's Horizon 2020 project h-ALO (photonic system for Adaptable muLtiple-analyte Monitoring of fOod quality), grant agreement No 101016706" and by the European Union – FSE REACT-EU, PON Ricerca e Innovazione 2014-2020, funding number F11B21009090007.

Institutional Review Board Statement: Not applicable.

 doi:10.20944/preprints202403.1082.v1

Informed Consent Statement: Not applicable.
Data Availability Statement: Not applicable.

Conflicts of Interest: The authors declare no conflict of interest.

Appendix A

Appendix A.1. Surface Plasmon Polariton Dispersion

The SPP dispersion relation were calculated using the simple theoretical model reported by Giudicatti in [29].The energies of the SPPs are determined by the following equation:

$$E(\theta, \Phi) = \hbar c \sqrt{\frac{\varepsilon_{gold}(E)+\varepsilon_d}{\varepsilon_{gold}(E)*\varepsilon_d}} |k_0(\Phi) \sin\theta + q_{mn}| \quad (1)$$

where ε_d represents the permittivity of the dielectric medium interfacing with the gold surface, q_{mn} denotes the reciprocal lattice vectors for the hexagonal lattice (Figure A3), and $k_0 \sin\theta$ is the in-plane wavevector of the incident light. The azimuthal angle Φ in this context accounts for the lattice orientation.

Appendix A.2. Variable-Angle Spectra

Figure A1 and A2 show the variable-angle R and T spectra, respectively, acquired by impinging from the front side (panels (a), (b)) and from the back side of the sample (panels (c) and (d) for different light polarization (TE or TM). Figure A3 reports the A maps calculated from the R and T spectra. In both cases, the red line indicates the He-Ne CW laser line at 632 nm.

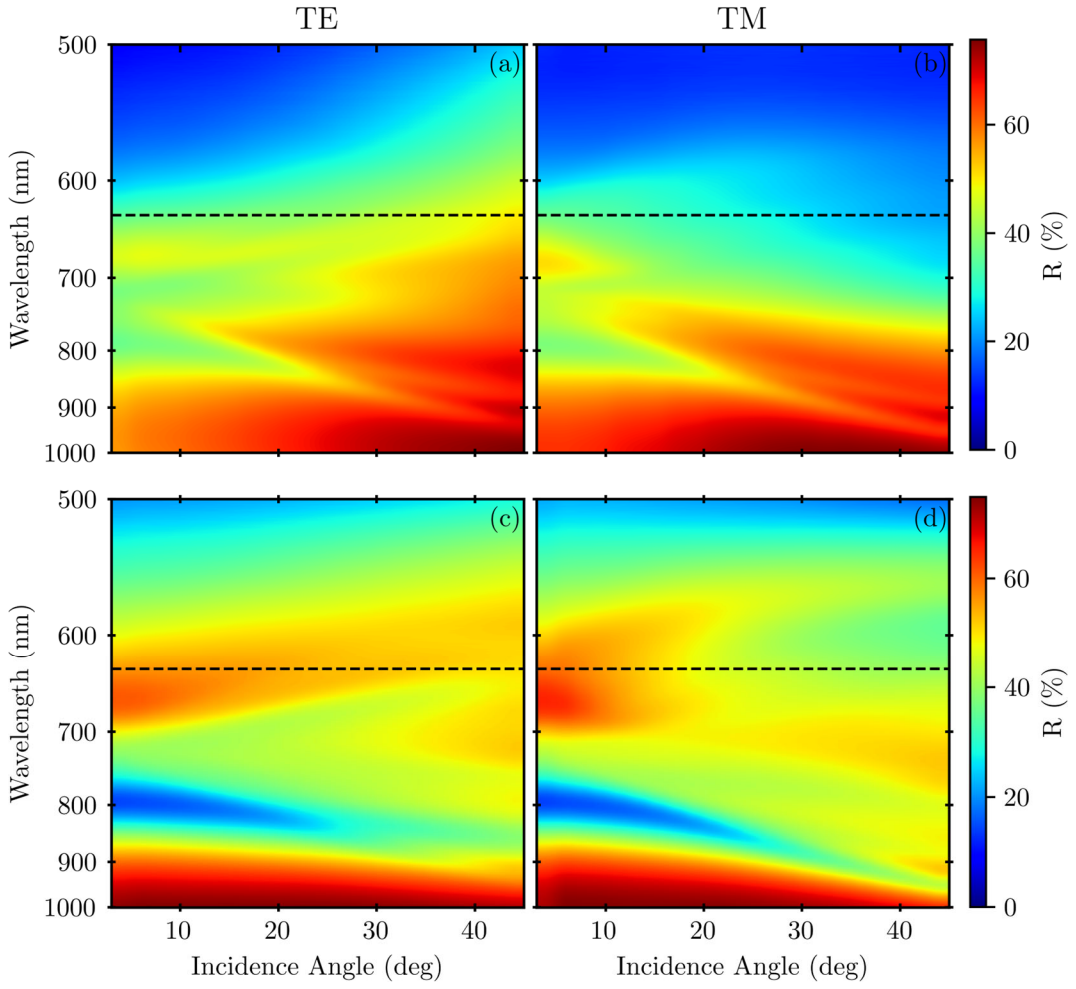

Figure A1. Variable-incidence-angle R spectra for both TE and TM polarization. Panels (a) and (b) display the curves resulting from the spectra measured by impinging with the white source from the

 doi:10.20944/preprints202403.1082.v1

front side of the sample, while panels (c) and (d) from the back side, respectively. The black dashed line indicates the pumping laser line at 632 nm.

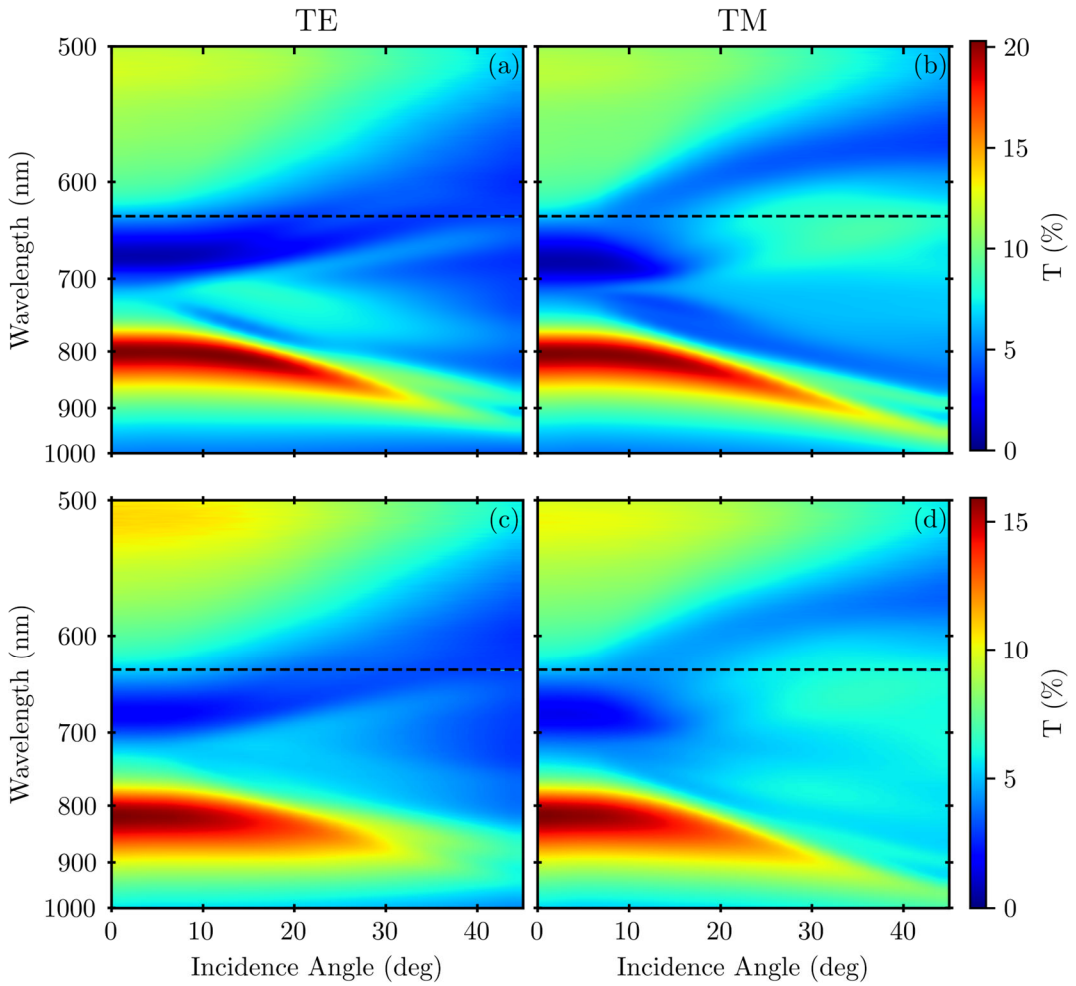

Figure A2. Variable-incidence-angle T spectra for both TE and TM polarization. Panels (a) and (b) display the curves resulting from the spectra measured by impinging with the white source from the front side of the sample, while panels (c) and (d) from the back side, respectively. The black dashed line indicates the pumping laser line at 632 nm.

 doi:10.20944/preprints202403.1082.v1

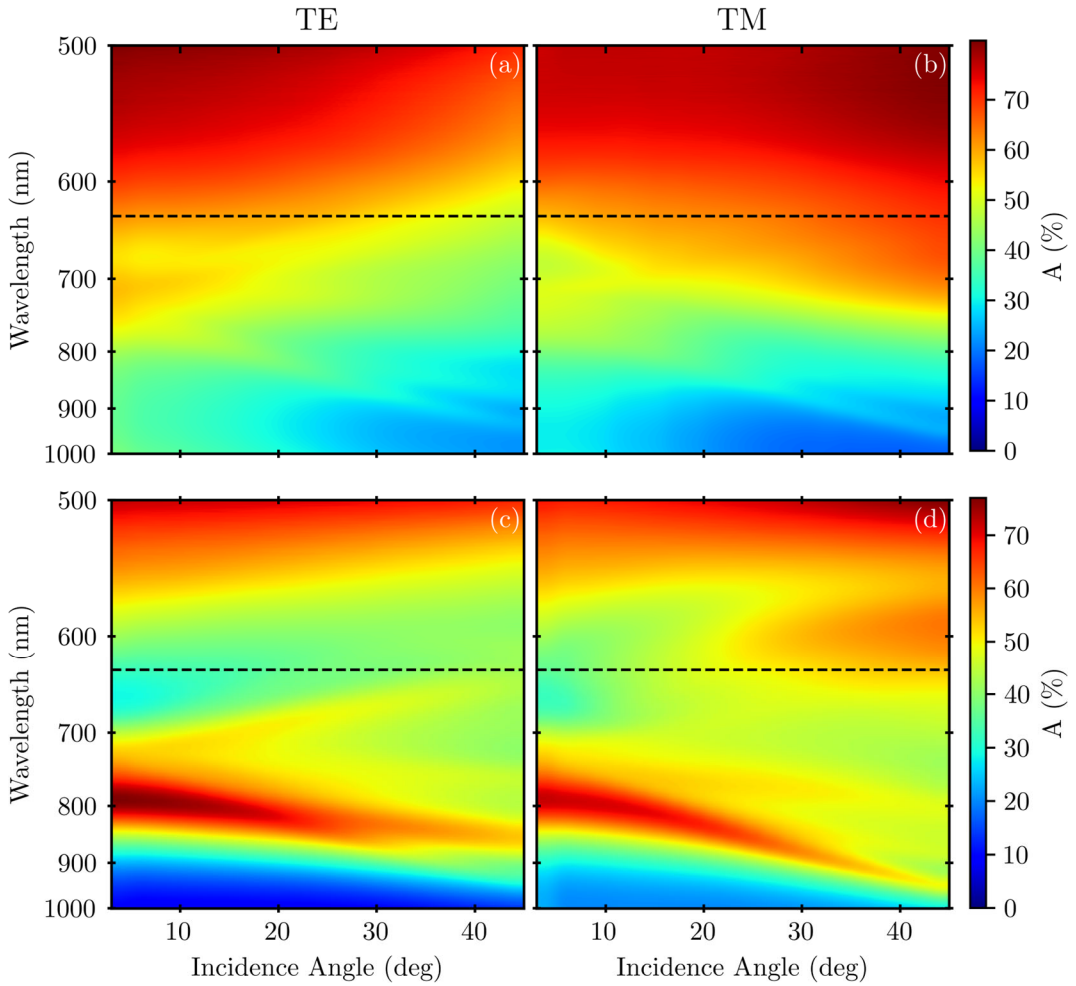

Figure A3. Calculated variable-incidence-angle A spectra for both TE and TM polarization. Panels (a) and (b) display the curves resulting from the spectra measured by impinging with the white source from the front side of the sample, while panels (c) and (d) from the back side, respectively. The black dashed line indicates the pumping laser line at 632 nm.

References

1. Jack George Calvert; James N. Pitts *Photochemistry*; Wiley, 1966; Vol. 378;.
2. Chance, R.R.; Prock, A.; Silbey, R. Molecular Fluorescence and Energy Transfer Near Interfaces. In *Advances in Chemical Physics*; Prigogine, I., Rice, S.A., Eds.; John Wiley & Sons, Inc.: Hoboken, NJ, USA, 1978; Vol. XXXVII, pp. 1–65.
3. Barnes, W.L. Fluorescence near Interfaces: The Role of Photonic Mode Density. 39.
4. Ford, G.W.; Weber, W.H. Electromagnetic Interactions of Molecules with Metal Surfaces. *Physics Reports* **1984**, *113*, 195–287, doi:10.1016/0370-1573(84)90098-X.
5. Kitson, S.C.; Barnes, W.L.; Sambles, J.R. Surface-Plasmon Energy Gaps and Photoluminescence. *Phys. Rev. B* **1995**, *52*, 11441–11445, doi:10.1103/PhysRevB.52.11441.
6. Liebermann, T.; Knoll, W. Surface-Plasmon Field-Enhanced Fluorescence Spectroscopy. *Colloids and Surfaces A: Physicochemical and Engineering Aspects* **2000**, *171*, 115–130, doi:10.1016/S0927-7757(99)00550-6.
7. Lakowicz, J.R. Radiative Decay Engineering: Biophysical and Biomedical Applications. *Analytical Biochemistry* **2001**, *298*, 1–24, doi:10.1006/abio.2001.5377.
8. Geddes, C.D.; Lakowicz R. Metal-Enhanced Fluorescence. *J. Fluoresc.* **2002**, *15*, 124–129.
9. Lakowicz, J.R. Radiative Decay Engineering 5: Metal-Enhanced Fluorescence and Plasmon Emission. *Analytical Biochemistry* **2005**, *337*, 171–194, doi:10.1016/j.ab.2004.11.026.
10. Fort, E.; Grésillon, S. Surface Enhanced Fluorescence. *J. Phys. D: Appl. Phys.* **2008**, *41*, 013001, doi:10.1088/0022-3727/41/1/013001.
11. Bauch, M.; Toma, K.; Toma, M.; Zhang, Q.; Dostalek, J. Plasmon-Enhanced Fluorescence Biosensors: A Review. **2014**, 19.

12. Osorio-Román, I.O.; Guerrero, A.R.; Albella, P.; Aroca, R.F. Plasmon Enhanced Fluorescence with Aggregated Shell-Isolated Nanoparticles. *Anal. Chem.* **2014**, *86*, 10246–10251, doi:10.1021/ac502424g.
13. Dong, J.; Zhang, Z.; Zheng, H.; Sun, M. Recent Progress on Plasmon-Enhanced Fluorescence. *Nanophotonics* **2015**, *4*, 472–490, doi:10.1515/nanoph-2015-0028.
14. Li, J.-F.; Li, C.-Y.; Aroca, R.F. Plasmon-Enhanced Fluorescence Spectroscopy. *Chem. Soc. Rev.* **2017**, *46*, 3962–3979, doi:10.1039/C7CS00169J.
15. Jeong, Y.; Kook, Y.-M.; Lee, K.; Koh, W.-G. Metal Enhanced Fluorescence (MEF) for Biosensors: General Approaches and a Review of Recent Developments. *Biosensors and Bioelectronics* **2018**, *111*, 102–116, doi:10.1016/j.bios.2018.04.007.
16. Liu, Y.; Blair, S. Fluorescence Enhancement from an Array of Subwavelength Metal Apertures. *Opt. Lett.* **2003**, *28*, 507, doi:10.1364/OL.28.000507.
17. Andrew, P.; Barnes, W.L. Molecular Fluorescence above Metallic Gratings. *Phys. Rev. B* **2001**, *64*, 125405, doi:10.1103/PhysRevB.64.125405.
18. Jiang, Y.; Wang, H.-Y.; Wang, H.; Gao, B.-R.; Hao, Y.; Jin, Y.; Chen, Q.-D.; Sun, H.-B. Surface Plasmon Enhanced Fluorescence of Dye Molecules on Metal Grating Films. *J. Phys. Chem. C* **2011**, *115*, 12636–12642, doi:10.1021/jp203530e.
19. Garrett *, S.H.; Smith, L.H.; Barnes, W.L. Fluorescence in the Presence of Metallic Hole Arrays. *Journal of Modern Optics* **2005**, *52*, 1105–1122, doi:10.1080/09500340512331323457.
20. Lakowicz, J.R.; Ray, K.; Chowdhury, M.; Szmacinski, H.; Fu, Y.; Zhang, J.; Nowaczyk, K. Plasmon-Controlled Fluorescence: A New Paradigm in Fluorescence Spectroscopy. *Analyst* **2008**, *133*, 1308, doi:10.1039/b802918k.
21. Cui, X.; Tawa, K.; Hori, H.; Nishii, J. Tailored Plasmonic Gratings for Enhanced Fluorescence Detection and Microscopic Imaging. *Adv. Funct. Mater.* **2010**, *20*, 546–553, doi:10.1002/adfm.200901401.
22. Cui, X.; Tawa, K.; Kintaka, K.; Nishii, J. Enhanced Fluorescence Microscopic Imaging by Plasmonic Nanostructures: From a 1D Grating to a 2D Nanohole Array. *Adv Funct Materials* **2010**, *20*, 945–950, doi:10.1002/adfm.200901993.
23. Langguth, L.; Punj, D.; Wenger, J.; Koenderink, A.F. Plasmonic Band Structure Controls Single-Molecule Fluorescence. *ACS Nano* **2013**, *7*, 8840–8848, doi:10.1021/nn4033008.
24. Chan, K.F.; Hui, K.C.; Li, J.; Fok, C.H.; Ong, H.C. Roles of Surface Plasmon Polaritons in Fluorescence Enhancement. In *Surface Plasmon Enhanced, Coupled and Controlled Fluorescence*; Geddes, C.D., Ed.; John Wiley & Sons, Inc.: Hoboken, NJ, USA, 2017; pp. 91–109 ISBN 978-1-119-32516-1.
25. Min, Jouha; Son, Taehwang; Hong, Jae-Sang; Cheah, Pike See; Wegemann, Andreas; Murlidharan, Koushik; Weissleder, Ralph; Lee, Hakho; Im, Hyungsoon Plasmon-Enhanced Biosensing for Multiplexed Profiling of Extracellular Vesicles. *Adv. Biosys.* **2020**, *4*, 2000003, doi:https://doi.org/10.1002/adbi.202000003.
26. Izumi, S.; Yamamura, S.; Hayashi, N.; Toma, M.; Tawa, K. Dual-Color Fluorescence Imaging of EpCAM and EGFR in Breast Cancer Cells with a Bull's Eye-Type Plasmonic Chip. **2017**, 10.
27. Zhang, Q.; Wu, L.; Wong, T.I.; Zhang, J.; Liu, X.; Zhou, X.; Bai, P.; Liedberg, B.; Wang, Y. Surface Plasmon-Enhanced Fluorescence on Au Nanohole Array for Prostate-Specific Antigen Detection. *IJN* **2017**, *Volume 12*, 2307–2314, doi:10.2147/IJN.S128172.
28. Semeniak, D.; Cruz, D.F.; Chilkoti, A.; Mikkelsen, M.H. Plasmonic Fluorescence Enhancement in Diagnostics for Clinical Tests at Point-of-Care: A Review of Recent Technologies. *Advanced Materials* **2023**, *35*, 2107986, doi:10.1002/adma.202107986.
29. Giudicatti, S.; Valsesia, A.; Marabelli, F.; Colpo, P.; Rossi, F. Plasmonic Resonances in Nanostructured Gold/Polymer Surfaces by Colloidal Lithography: Plasmonic Resonances in Nanostructured Gold/Polymer Surfaces. *phys. stat. sol. (a)* **2010**, *207*, 935–942, doi:10.1002/pssa.200925579.
30. Giudicatti, S.; Marabelli, F.; Valsesia, A.; Pellacani, P.; Colpo, P.; Rossi, F. Interaction among Plasmonic Resonances in a Gold Film Embedding a Two-Dimensional Array of Polymeric Nanopillars. *J. Opt. Soc. Am. B* **2012**, *29*, 1641, doi:10.1364/JOSAB.29.001641.
31. Bottazzi, B.; Fornasari, L.; Frangolho, A.; Giudicatti, S.; Mantovani, A.; Marabelli, F.; Marchesini, G.; Pellacani, P.; Therisod, R.; Valsesia, A. Multiplexed Label-Free Optical Biosensor for Medical Diagnostics. *J. Biomed. Opt* **2014**, *19*, 017006, doi:10.1117/1.JBO.19.1.017006.
32. Available online : Https://H-Alo.Eu/ (accessed on 30 January 2024).
33. Angelini, M.; Manobianco, E.; Pellacani, P.; Floris, F.; Marabelli, F. Plasmonic Modes and Fluorescence Enhancement Coupling Mechanism: A Case with a Nanostructured Grating. *Nanomaterials* **2022**, *12*, 4339, doi:10.3390/nano12234339.
34. Angelini, M.; Manobianco, E.; Pellacani, P.; Floris, F.; Marabelli, F. Refractive Index Dependence of Fluorescence Enhancement in a Nanostructured Plasmonic Grating. *Materials* **2023**, *16*, 1289, doi:10.3390/ma16031289.
35. Glinel, K.; Moussa, A.; Jonas, A.M.; Laschewsky, A. Influence of Polyelectrolyte Charge Density on the Formation of Multilayers of Strong Polyelectrolytes at Low Ionic Strength. *Langmuir* **2002**, *18*, 1408–1412, doi:10.1021/la0113670.

 doi:10.20944/preprints202403.1082.v1

36. Nicol, E.; Habib-Jiwan, J.-L.; Jonas, A.M. Polyelectrolyte Multilayers as Nanocontainers for Functional Hydrophilic Molecules. *Langmuir* **2003**, *19*, 6178–6186, doi:10.1021/la034855b.